J. Fluid Mech. (2002), *vol.* 465, *pp.* 331–352.
DOI: 10.1017/S0022112002001088 Printed in the United Kingdom

Vorticity transport in a corner formed by a solid wall and a free surface

By L. M. GREGA[1], T. Y. HSU[2] AND T. WEI[2]

[1]Department of Mechanical Engineering, The College of New Jersey Ewing, NJ 08628, USA

[2]Department of Mechanical and Aerospace Engineering, Rutgers;
The State University of New Jersey, Piscataway, NJ 08854-8058, USA

(Received 28 June 2000 and in revised form 6 February 2002)

There is a growing body of literature in which turbulent boundary layer flow along a mixed-boundary corner formed by a vertical solid wall and a horizontal free surface has been examined. While there is consensus regarding the existence of weak secondary flows in the near corner region, there is some disagreement as to the exact nature and origin of these flows. In two earlier works by the authors, evidence was presented supporting the existence of a weak streamwise vortex which rotates in toward the wall at the free surface and down away from the surface along the wall. This 'inner secondary vortex' is accompanied by an 'outer secondary flow' which transports low-momentum boundary layer fluid up along the wall and outward at the free surface. The magnitudes of the cross-stream velocities associated with these secondary flows were measured to be on the order of 1% of the free-stream speed. In this paper, high-resolution DPIV measurements made in the cross-stream plane are presented. These clearly show the inner and outer secondary flows. The cross-stream vector fields allow computation of terms in the turbulent streamwise vorticity transport equation. These terms indicate mean vorticity transport at the free surface associated with the outer secondary flow. In addition there appears to be a balance between the wall-normal and free-surface-normal fluctuating vorticity reorientation terms.

1. Introduction

In the last few years, turbulence associated with the horizontal flow of water along a vertical wall in the vicinity of a horizontal free surface, the 'mixed-boundary corner', has received much of attention. Examples of recent works include experimental studies by Grega *et al.* (1995), Longo, Huang & Stern (1998), and Hsu *et al.* (2000), and large-eddy simulation studies by Thomas & William (1995) and Sreedhar & Stern (1998). The motivation for these studies ranged from modelling ship wakes through transport in rivers and channels, to anisotropies in manufacturing processes such as papermaking.

A common finding in those studies is evidence of weak secondary flows, which are believed to result from anisotropic boundary conditions. These secondary flows appear to be similar to features reported by Gessner & Jones (1961, 1965) for turbulent flow along a solid–solid corner, and by Logory, Hirsa & Anthony (1996) for the wake of a surface-piercing plate. One of the basic open issues yet to be resolved, however, is the exact nature of the secondary flows. There appears to be consensus regarding the existence of some sort of streamwise vortex in the near corner region. However

the size, strength, and even sense of rotation have not been established; certainly the origins of this vortex have not been established. There is also general agreement regarding the existence of a surface current that transports low-momentum boundary layer fluid up along the wall and then away from the wall at the free surface. Again, however, the nature of this flow has not been clearly demonstrated.

Much of the confusion is probably due to differences between the different studies. These differences were detailed in Hsu *et al.* (2000). Briefly stated, experiments reported by the present authors were conducted along the sidewall of a large free-surface water tunnel where the flow may be assumed to be fully evolved with only weak variations in the stream direction. By contrast, the experiments of Longo *et al.* (1998) were for a towed surface-piercing plate with limited run time. It is possible that they were measuring the early, temporally evolving development of the secondary flows. In their concurrent simulations, Sreedhar & Stern (1998) employed a compressible RANS code for which it is not clear that a comparison to their surface-piercing plate results is even appropriate. Indeed, comparisons in Hsu *et al.* (2000) showed dramatic differences between the results from the Rutgers experiments and Sreedhar & Stern's (1998) computations.

The objective of the present study, therefore, was to use direct high-resolution measurements of the cross-stream plane in the mixed-boundary corner to definitively document the secondary flows. It was further hoped that acquisition of such data would shed light on the origins of these flows. Specifically, highly resolved, statistically convergent two-dimensional velocity field data would directly reveal the form, strength, and extent of the mixed-boundary corner flows. Further, these measurements could be used to compute terms in the streamwise vorticity transport equation. This paper documents the results from this experiment.

2. A working model of mixed-boundary corner secondary flows

In Grega *et al.* (1995) and Hsu *et al.* (2000), a working model of secondary flows formed in a mixed-boundary corner was developed. A schematic diagram appears in figure 1. As shown in the drawing, the inner secondary vortex is weak, with flow in toward the wall at the free surface and down away from the free surface along the wall. This is analogous to secondary vortices found in flow along a corner formed by two solid walls. Like the solid–solid corner, circumferential velocities in the solid–free-surface corner vortex are on the order of 1% of the mean stream speed. Thus, the inner secondary vortex is essentially a mean phenomenon; one would not expect to see such a vortex in an instantaneous cross-stream measurement.

Evidence supporting the existence of this inner secondary vortex was obtained for a narrow channel using DNS. Those findings were presented in Grega *et al.* (1995). The inner vortex was found to be $\sim$100 viscous units in diameter with maximum circumferential velocities on the order of 1% of the free-stream speed. Like the schematic in figure 1, the inner secondary vortex was located close to the mixed-boundary corner. Experimental data were also presented, both in Grega *et al.* (1995) and Hsu *et al.* (2000). These results however, were obtained in planes parallel to the free surface; there was insufficient resolution in the free-surface-normal direction to conclusively map the inner secondary flows.

There is also no complete picture, either computational or experimental, of the outer secondary flow shown in figure 1. In the DNS study reported in Grega *et al.* (1995), the channel half-width was only 150 viscous units. A symmetry boundary condition was imposed on the domain boundary opposite the no-slip wall. The free

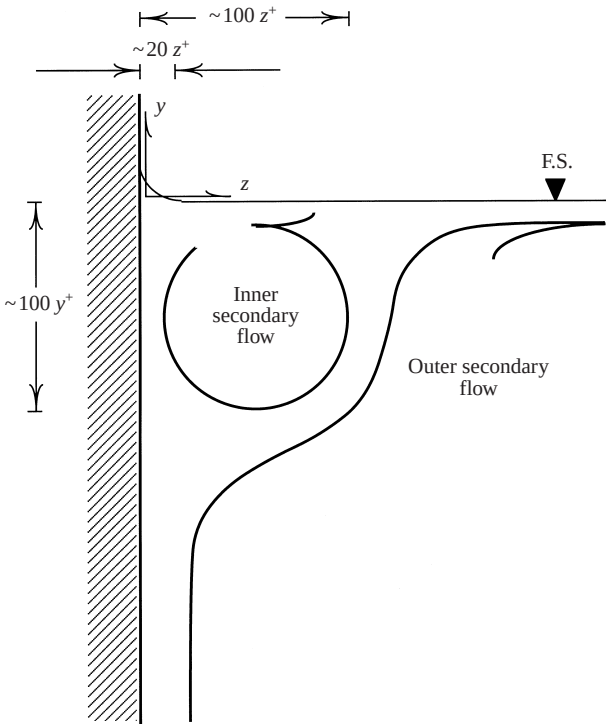

FIGURE 1. Schematic drawing of the hypothesized secondary flow patterns in a mixed-boundary corner.

surface was represented as a shear-free boundary. Because of this limited width, it was not possible to develop and resolve a free-surface current characteristic of many free-surface turbulent flows. Instead, the DNS results indicated the formation of a second 'outer' secondary flow directly below the 'inner', i.e. near corner, vortex.

By contrast, the centreline of the water tunnel used for the present experiments, and those of Grega *et al.* (1995) and Hsu *et al.* (2000), was $\sim$ 2700 viscous lengths from the test section sidewalls. This clearly was sufficiently large to permit development of the outer secondary flow, also shown in figure 1. As discussed in the two earlier papers, this outer secondary flow is the mean surface current responsible for transverse spreading of turbulence at the free surface. In this flow, turbulent boundary layer fluid is transported up toward the free surface along the wall, around the inner secondary vortex and out away from the wall at the free surface. Free-surface currents of this type have been reported for wake flows by Logory *et al.* (1996) and for near-surface jets by Anthony & Willmarth (1992). For broader discussions of free-surface currents, the reader is referred to Sarpkaya (1996) and Walker, Leighton & Garza-Rios (1996).

As noted in this and the preceding section, there is, as yet, no conclusive validation (or refutation) of the hypothesized secondary flow patterns shown in figure 1. However, with the availability of high-resolution DPIV measurement capabilities, direct measurement of the flow is possible. There are, of course, significant experimental difficulties in making these measurements, including measurement resolution, adequate sampling, parallax, etc. Thus, a significant component of this work lies in demonstrating the accuracy of the reported measurements. For continuity, however, details of measurement accuracy and parallax correction have been put into Appendices.

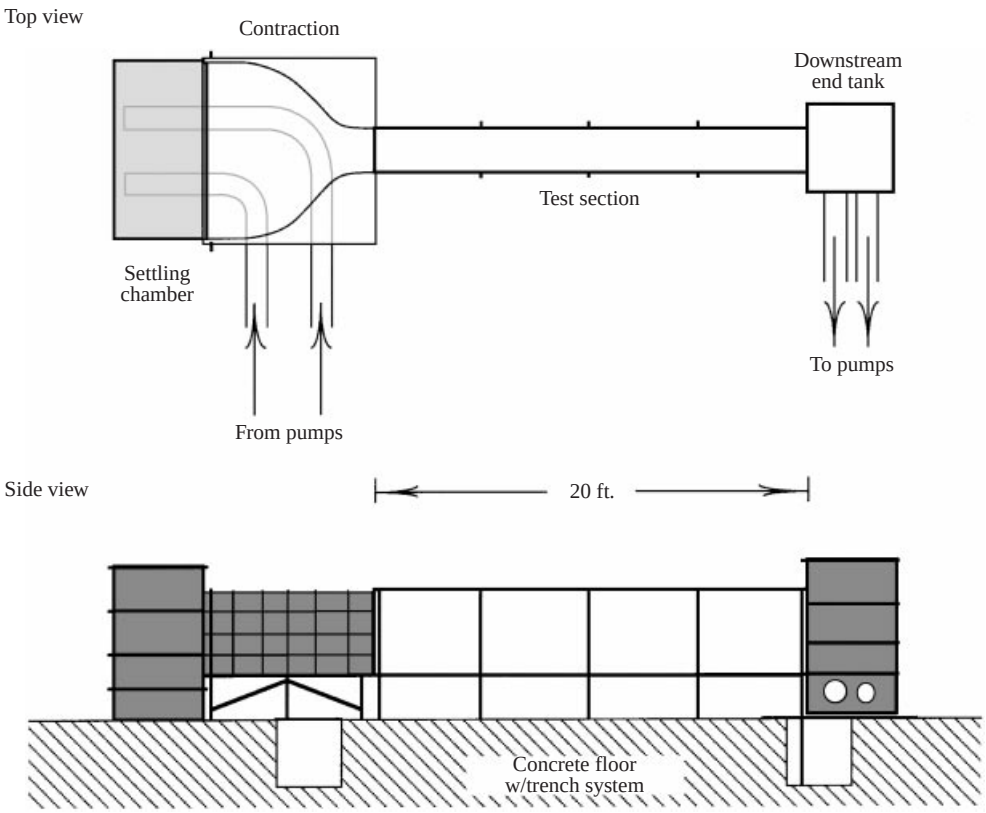

FIGURE 2. Top and side view schematics of the free-surface water tunnel. Note that the pumps are not shown.

3. Experimental apparatus and methods

Measurements reported in this paper are an extension of experiments previously reported in Grega *et al.* (1995) and Hsu *et al.* (2000); the distinguishing feature of the present data was the cross-stream measurement plane. Therefore, the experimental apparatus and methods are only briefly outlined here. For detailed descriptions of the facility and methodology, please refer to Smith (1992), Grega *et al.* (1995), Hsu (1999), and Hsu *et al.* (2000).

Experiments were conducted along one sidewall of the large free-surface water tunnel at Rutgers. Top and side view drawings of the tunnel are shown in figure 2. The test section measured 58.4 cm in width $\times$ 122 cm in depth $\times$ 610 cm in length. The maximum free-stream velocity with the test section filled was $\sim 30\,\mathrm{cm\,s^{-1}}$. Free-stream turbulence levels were less than 0.1%.

For this study, the free-stream velocity was $12\,\mathrm{cm\,s^{-1}}$, corresponding to a Reynolds number based on momentum thickness, Re_θ, of 670. The friction velocity, u_τ, at the tunnel mid-height was $0.63\,\mathrm{cm\,s^{-1}}$, and the kinematic viscosity was $0.010\,\mathrm{cm^2\,s^{-1}}$. (It should be noted here that Grega *et al.* 1995 and Hsu *et al.* 2000 documented variations in friction velocity with depth close to the free surface. These variations are due to boundary layer thickening associated with the outward free-surface current. For this study, data were scaled using the friction velocity corresponding to the canonical boundary layer at the tunnel mid-height, i.e. $u_\tau = 0.63\,\mathrm{cm\,s^{-1}}$.)

Measurements were made along one of the test section sidewalls ~ 380 cm down-

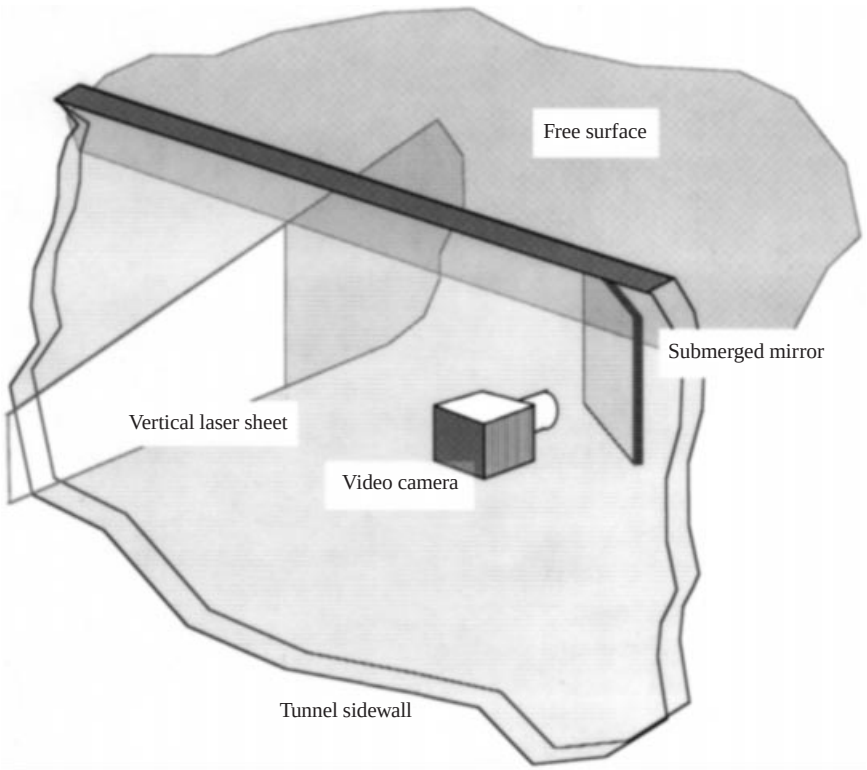

FIGURE 3. Oblique view drawing showing the measurement configuration. The vertical laser sheet, front-surface mirror oriented at 45° to the flow and digital video camera are shown.

stream of the inlet. A schematic drawing showing the DPIV optics appears in figure 3. The drawing shows a laser sheet aimed through the test section sidewall to illuminate a y, z section immediately below the free surface; care was taken to avoid reflections from the free surface. Next, a front surface mirror, oriented at 45° to the flow direction, was placed along the sidewall ~ 60 cm downstream of the laser sheet. This mirror permitted viewing of seeding particles passing through the laser sheet. Finally, the video camera was placed opposite the mirror so that the reflected image of the laser sheet filled the field of view.

High-resolution digital particle image velocimetry (DPIV) video images were generated using a Coherent Innova 70-5 argon-ion laser, a Texas Instruments TI-1134MP black and white digital video camera, and a laser sweep circuit developed for these measurements. The sweep circuit was used to rotate a small mirror, mounted on the shaft of a galvanometer, to illuminate the flow at the end of one video frame and again at the beginning of the next frame. The time between sweeps comprising a DPIV video image pair, Δt, was 4.4 ms. The flow was seeded with 3 μm titanium dioxide particles. The field of view of the camera for these studies was 2.14 cm (vertical) × 2.88 cm (horizontal). This corresponds to 120 viscous lengths in the free-surface-normal direction and 160 viscous lengths in the wall-normal direction.

DPIV image processing software was identical to that reported in Hsu *et al.* (2000). The program employed a two-stage correlation algorithm in which a large interrogation window was used for a highly accurate, though spatially averaged, coarse displacement field. This was followed by a refined correlation stage in which

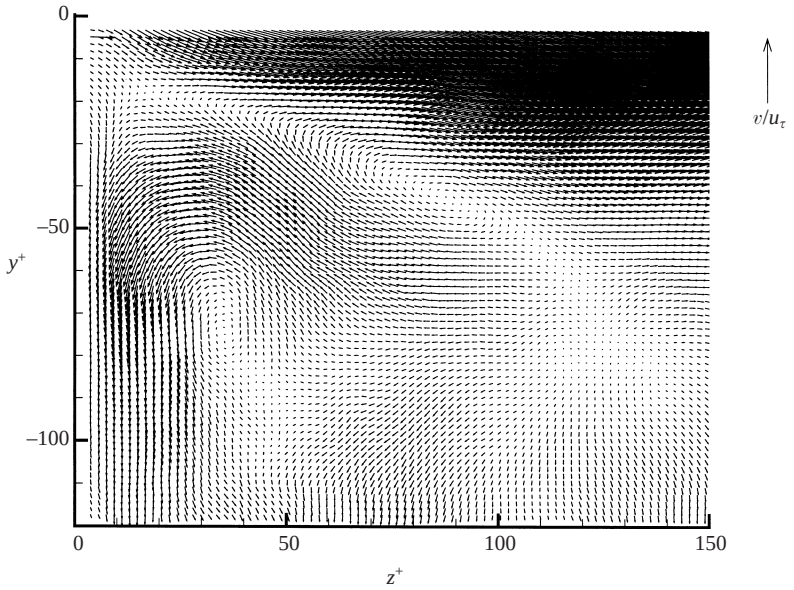

FIGURE 4. Mean cross-stream velocity field with parallax correction applied.

corresponding interrogation windows were displaced by an amount prescribed by the coarse displacement field. As in Hsu *et al.* (2000), one thousand instantaneous DPIV image pairs were captured at ~ 2 s intervals for a total sampling time in excess of 30 mins. The fine correlation windows were 24×48 pixels with four times over-sampling. A detailed discussion of uncertainties appears in Appendix B.

Before proceeding, it is important to note that nonlinear parallax effects were significant. The nonlinearity arose because measurements were made in a boundary layer where streamwise velocity varied strongly with distance from the wall. To remove this effect, a parallax correction was developed. Details of this correction are presented in Appendix A.

4. Results and discussion

This section contains spatially resolved measurements of secondary flow patterns in a turbulent mixed-boundary corner flow. As discussed in § 1, the existence, form and origins of the secondary flows are still open research issues. The fundamental difficulty in mapping these patterns is that turbulence masks the underlying mean flow; velocity magnitudes associated with the secondary flows are estimated to be on the order of 1% of the free-stream speed. Thus, highly resolved and highly accurate measurements are required to extract mean secondary motions from the over-riding turbulence. The present data represent the first known direct mapping of these secondary flows. In making these measurements, however, it was also possible to obtain cross-stream turbulence data along with terms in the turbulent streamwise vorticity transport equation. These results are presented along with thoughts on the origins of the secondary flows.

Figure 4 shows the mean cross-stream velocity vector field in the mixed-boundary corner. The solid wall appears along the left edge of the plot, while the free surface is located along the top edge. The bulk flow direction in this and all subsequent figures is into the page. The free-surface-normal and wall-normal directions are defined to

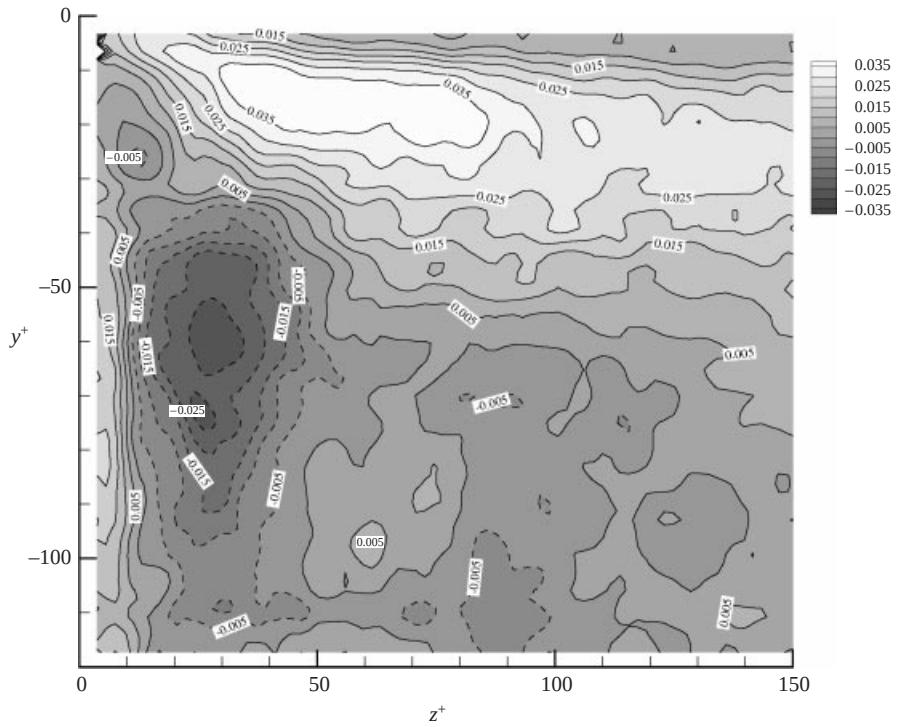

FIGURE 5. Mean streamwise vorticity field scaled on inner variables. Dotted contours denote negative values. Contour labels provide magnitude information.

be y and z, respectively. To maintain a right-hand coordinate system with streamwise velocity into the page, distances below the free surface are negative.

The presence of weak mean secondary flows are clearly evident in figure 4; a reference vector corresponding to $v/u_\tau = 1$ appears to the right of the plot for comparison. For further clarification, a contour plot of mean streamwise vorticity is shown in figure 5. From these plots, one can see the 'inner secondary vortex' centred approximately at $y^+ \approx -75$ and $z^+ \approx 35$. The counter-clockwise sense of rotation, i.e. negative vorticity, is consistent with DNS calculations and experimental observations presented in Grega *et al.* (1995) and Hsu *et al.* (2000).

The free-surface current, which transports low-momentum boundary layer fluid away from the wall close to the free surface, is also distinctly visible in both figures 4 and 5. In figure 5, this 'outer secondary flow' manifests itself as a horizontal band of positive streamwise vorticity. Vorticity exists in this case because the region of positive mean wall-normal velocity W occurs only close to the free surface; farther from the surface, W tends to zero.

Figure 6 contains contour plots of wall-normal and free-surface-normal turbulence intensities, w'/u_τ and v'/u_τ, respectively. The wall-normal data agree quite well with measurements, presented in Hsu *et al.* (2000), obtained from horizontal (x, z)-plane DPIV measurements; direct comparisons are included in Appendix B. Key features described in Hsu *et al.* (2000) are also visible here. For example, observe that for a fixed distance from the wall, w'/u_τ decreases approaching the free surface. However, close to the wall, w'/u_τ rebounds slightly for $-20 \leqslant y^+ \leqslant 0$. It was hypothesized in Hsu *et al.* (2000) that this was due to a dramatic decrease in dissipation close to the free surface.

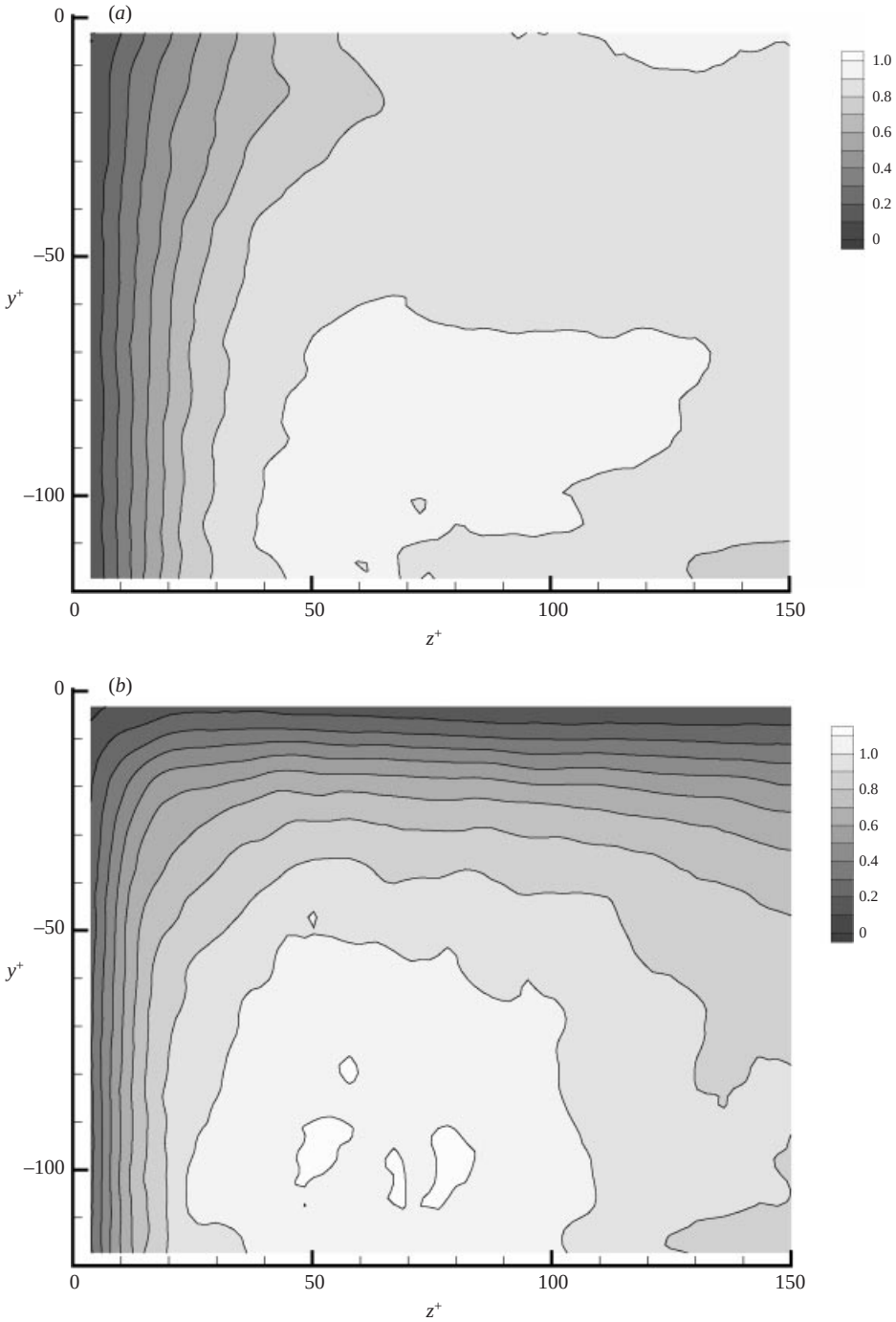

FIGURE 6. (*a*) Wall-normal turbulence intensities, w'/u_τ, and (*b*) free-surface-normal turbulence intensities, v'/u_τ.

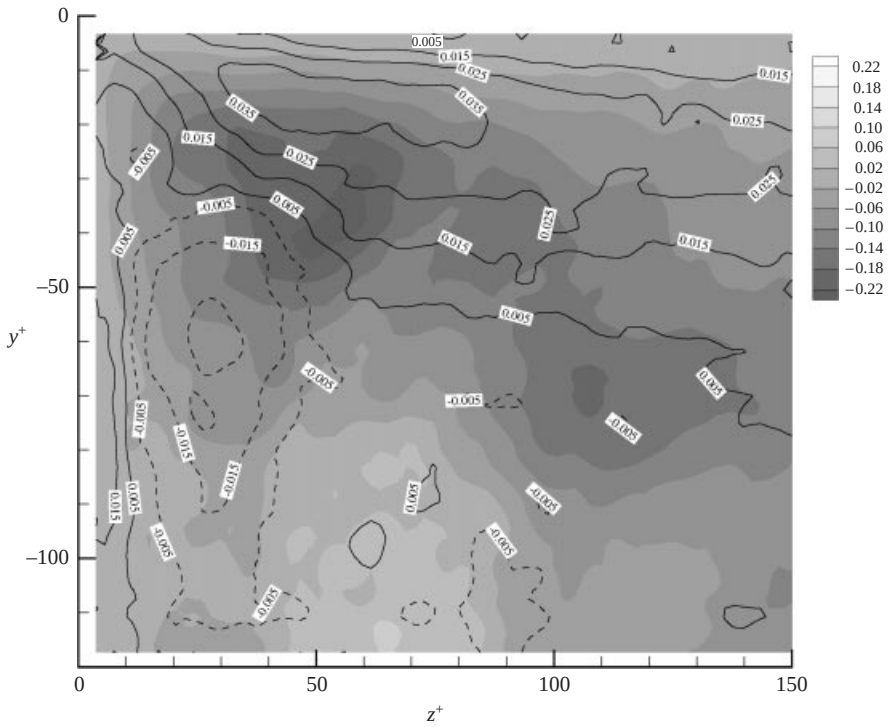

FIGURE 7. Cross-stream Reynolds stress, $-\langle vw\rangle/u_\tau^2$. Contours of mean cross-stream vorticity, including magnitude labels, are overlaid for comparison.

A contour plot of cross-stream Reynolds stress, $-\langle vw\rangle/u_\tau^2$, is shown in figure 7. The salient feature of this figure is the patch of comparatively large Reynolds stress coinciding with the boundary between the inner and outer secondary flows. For ease of reference, iso-vorticity contours from figure 5 are presented as solid lines. In this region, the magnitudes of $-\langle vw\rangle/u_\tau^2$ are approximately 0.2. By comparison, the maximum magnitudes of the dominant Reynolds stress component, $-\langle uw\rangle/u_\tau^2$, are ~ 0.8. Thus, unlike a canonical boundary layer, cross-stream turbulent momentum exchange is significant in the mixed-boundary corner.

The existence of anisotropic Reynolds stress distributions, particularly in the (y, z)-plane, raises the issue of the origin of the secondary flows. In Gessner & Jones (1965), weak streamwise vortices in the near corner region of a turbulent flow along a solid–solid corner were hypothesized to result from anisotropic turbulent stresses. To develop this argument, Gessner & Jones (1965) employed the mean turbulent streamwise vorticity equation:

$$\frac{\mathrm{D}\Omega_x}{\mathrm{D}t} = \Omega_x\frac{\partial U}{\partial x} + \Omega_y\frac{\partial U}{\partial y} + \Omega_z\frac{\partial U}{\partial z} + \nu\nabla^2\Omega_x + \frac{\partial}{\partial x}\left\{\frac{\partial\langle uv\rangle}{\partial z} - \frac{\partial\langle uw\rangle}{\partial y}\right\}$$
$$+ \frac{\partial^2}{\partial y\partial z}\{\langle v^2\rangle - \langle w^2\rangle\} + \left\{\frac{\partial^2}{\partial z^2} - \frac{\partial^2}{\partial y^2}\right\}\langle vw\rangle. \qquad (1)$$

Here capital Ω_i and U denote mean vorticity and local mean streamwise velocity, while lower-case u, v and w indicate fluctuating velocities in the x-, y- and z-directions, respectively. The angle brackets denote ensemble averaging. This equation can be

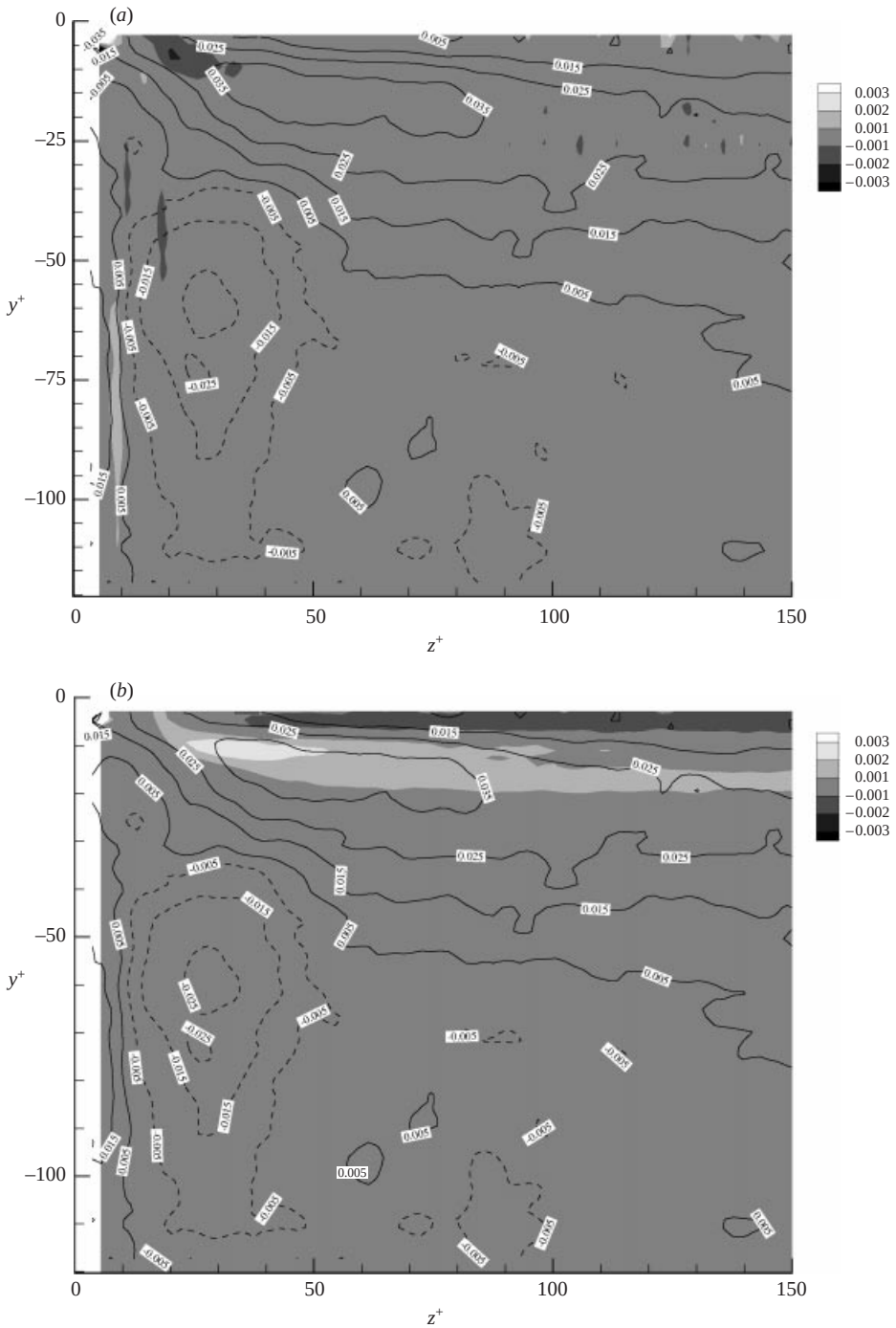

FIGURE 8 (*a*, *b*). For caption see facing page.

generated by first taking the curl of the turbulent momentum equations and then taking the mean. The left-hand side of the resulting equation represents rate of change of vorticity following a fluid element relative to an inertial reference frame. The first four terms on the right-hand side describe stretching, reorientation, and

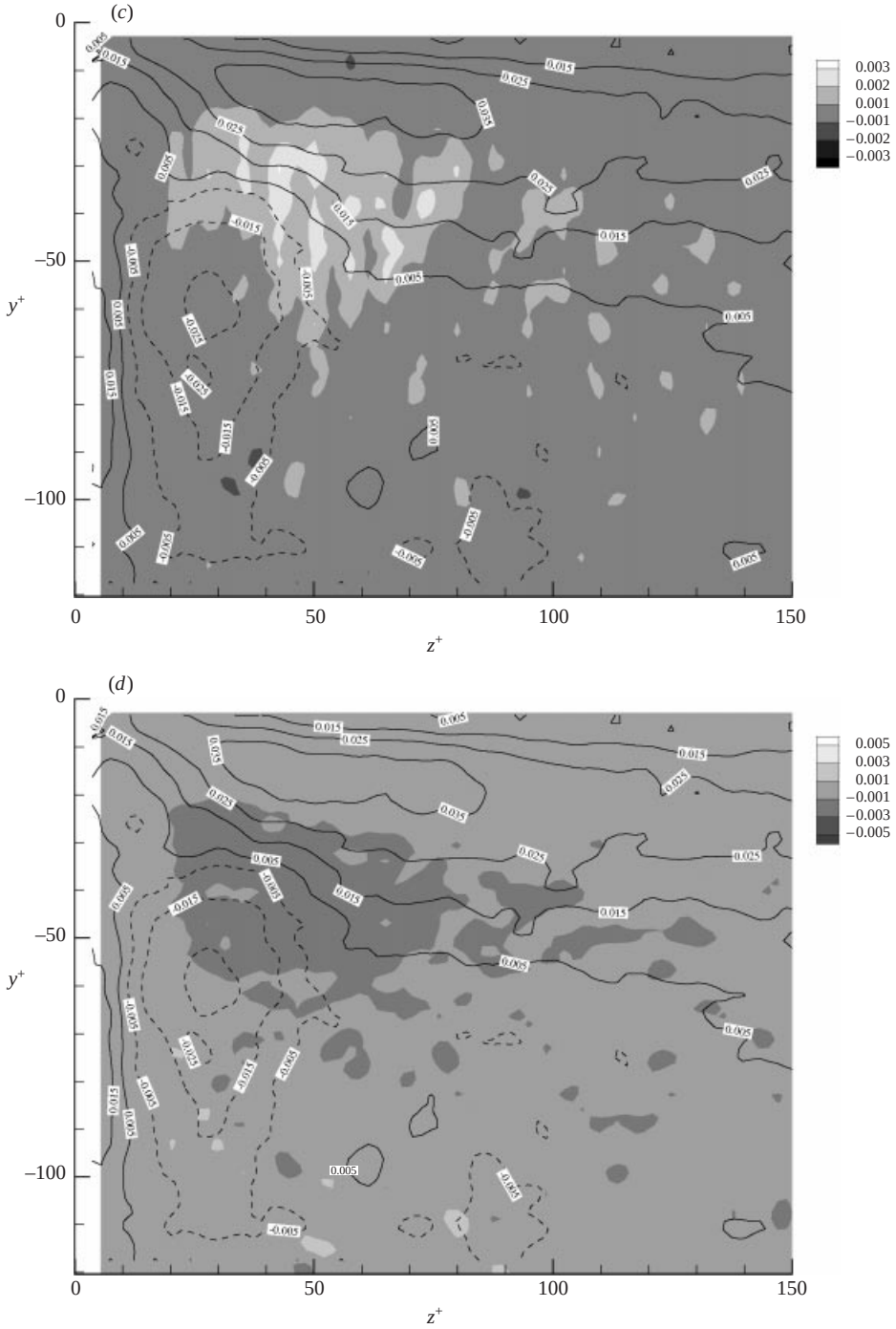

FIGURE 8. (*a*) Transport of mean streamwise vorticity in the wall-normal direction by the mean flow, $W\partial\Omega_x/\partial z$. (*b*) Transport of mean streamwise vorticity in the free-surface-normal direction by the mean flow, $V\partial\Omega_x/\partial y$. (*c*) Transport of fluctuating streamwise vorticity in the wall normal direction by the turbulent flow, $w\partial\omega_x/\partial z$. (*d*) Transport of fluctuating streamwise vorticity in the free-surface-normal direction by the turbulent flow, $v\partial\omega_x/\partial y$. Again, mean cross-stream vorticity contours have been overlaid for comparison.

diffusion of mean vorticity by the mean flow. Finally, the last three terms represent vorticity production by anisotropic turbulent stresses. For isotropic turbulence, these final terms are identically zero.

An alternative representation of the mean turbulent streamwise vorticity equation appears in Tennekes & Lumley (1972):

$$\frac{\mathrm{D}\Omega_x}{\mathrm{D}t} + \left\langle \frac{\mathrm{D}\omega_x}{\mathrm{D}t} \right\rangle = \Omega_x \frac{\partial U}{\partial x} + \Omega_y \frac{\partial U}{\partial y} + \Omega_z \frac{\partial U}{\partial z} + \nu \nabla^2 \Omega_x + \left\langle \omega_x \frac{\partial u}{\partial x} \right\rangle + \left\langle \omega_y \frac{\partial u}{\partial y} \right\rangle + \left\langle \omega_z \frac{\partial u}{\partial z} \right\rangle, \tag{2}$$

where lower case, ω_i denotes fluctuating vorticity.

Note that one can obtain (1) from (2) by expanding all of the fluctuating terms and employing incompressible continuity to eliminate terms. In so doing, one finds that the anisotropic Reynolds stress terms in (1) are parts of the fluctuating vorticity advection term, $\langle \mathrm{D}\omega_x/\mathrm{D}t \rangle$, in (2). While the first anisotropy term, $(\partial/\partial x)\{\partial\langle uv\rangle/\partial z - \partial\langle uw\rangle/\partial y\}$, originates from the streamwise advection term, $u\partial\omega_x/\partial x$. The second and third terms, i.e. the last two terms in (1), are each formed by combining parts of the cross-stream advection terms, $\langle \omega_y \partial u/\partial y \rangle$ and $\langle \omega_z \partial u/\partial z \rangle$. In a sense, the anisotropic Reynolds stress gradient terms are decidedly non-physical. They are, however, commonly used by those studying the solid–solid corner problem; the normal stress gradient term, $(\partial^2/\partial y \partial z)\{\langle v^2 \rangle - \langle w^2 \rangle\}$, has been shown to be important. This does not appear to be the case for the mixed boundary corner problem. Indeed, all of the anisotropy terms were found to be negligibly small.

The distinct advantages of (2) over (1) are the comparative ease of physical interpretation of individual terms and the reduced resolution necessary to accurately compute the turbulence terms. In the alternative form, (2), one can readily interpret the fluctuating terms as the transport of fluctuating streamwise vorticity by the turbulent fluid motions (the additional terms on the left-hand side of the equation) and stretching and reorientation of turbulent vorticity by localized turbulent velocity gradients.

Of the terms in (2), six can be directly computed from cross-stream data, including the mean and fluctuating vorticity advection terms ($V\partial\Omega_x/\partial y$, $W\partial\Omega_x/\partial z$, $\langle v\partial\omega_x/\partial y\rangle$ and $\langle w\partial\omega_x/\partial z\rangle$), and two vorticity diffusion terms ($\nu\partial^2\Omega_X/\partial y^2$ and $\nu\partial^2\Omega_x/\partial z^2$). In addition, continuity was used to compute the stretching of mean streamwise vorticity by the mean axial strain field ($\Omega_x\partial U/\partial x$). These calculations indicate that the only significant terms in the streamwise vorticity transport equation for this flow were the four advection terms. It will be seen that even these quantities appear to be quite small. For the complete data set, readers are referred to Hsu (1999).

Figure 8 is a composite of shaded contour plots showing the four streamwise vorticity advection terms. Superimposed on each plot are line contours of mean streamwise vorticity. Again all data have been non-dimensionalized by friction velocity and kinematic viscosity. Mean transport in the wall-normal and free-surface-normal directions are shown in figure 8(a, b), while the respective fluctuating transport terms are shown in figure 8(c, d).

Figure 8(a, b) indicates that transport of mean vorticity by the mean flow occurs predominantly in the outer secondary region. That is, there is a horizontal band of vertical vorticity transport close to the free surface in figure 8(b). This can be explained by the coexistence of free-surface-normal velocity and vertical streamwise vorticity gradients along the free surface. There is evidence of mean vorticity transport

in the wall-normal direction along the wall as well, figure 6(*a*), but this is not as strong an effect.

In figure 8(*c*, *d*), there are patches of fluctuating vorticity advection in the near corner region, in the range $10 \leqslant z^+ \leqslant 70$ and $-10 \leqslant y^+ \leqslant -50$. From the overlaid vorticity contours, one can see that this region corresponds to the interface between the inner secondary vortex where $\Omega_x < 0$, and the outer secondary flow, i.e. the free-surface current, where $\Omega_x > 0$. Observe that the sign of the fluctuating wall-normal transport, figure 8(*c*), is positive, while the fluctuating free-surface-normal transport, figure 8(*d*), is negative; the two figures are otherwise roughly identical (in size, location and magnitude). Thus, it appears that there is no net transport of turbulent vorticity due to fluctuating velocities. Taken *in toto*, however, the four advection terms in figure 8 do not sum to zero. This implies that streamwise vorticity is being supplied through stretching and reorientation of cross-stream vorticity components, though data are not yet available to support this hypothesis.

5. Conclusion

High-resolution DPIV measurements were made in a cross-stream plane of a turbulent mixed-boundary corner flow. These measurements clearly resolved the inner and outer secondary flows which have been discussed, but not conclusively documented, in a series of studies spanning the last decade. In addition, terms in the turbulent streamwise vorticity transport equation were computed from the DPIV velocity fields. These results indicate that there is an, as yet, undetermined source of streamwise vorticity particularly in the outer secondary flow region close to the free-surface.

Partial support for this research from the Office of Naval Research (Grant#N00014-92-J-1020) through Dr Edwin P. Rood is gratefully acknowledged. The authors also acknowledge Mr Abram Voorhees for his help in obtaining data for the uncertainty analysis. Finally, we appreciate the helpful discussions with Dr Richard Leighton of the Naval Research Laboratory.

Appendix A. Parallax correction

As noted earlier, the unique feature of the present measurements was the use of a cross-stream laser sheet, i.e. in the (y, z)-plane, where y and z denote the free-surface and wall-normal directions, respectively. Use of this measurement plane, however, creates a parallax problem as seeding particles pass through the illuminating laser sheet. That is, because the camera imaging surface is smaller than the field of view, particles moving toward the camera appear to have a radial motion away from the central camera line-of-sight. This was particularly relevant in the current study because the mean secondary-flow velocities were on the same order as the parallax effect.

For a uniform flow, the parallax effect is an irrotational source flow where the parallax velocities are proportional to distance from the camera line-of-sight. In the present study, an additional correction is necessary because of spatial variations in mean streamwise velocity owing to the presence of the solid and free-surface boundaries. For shear flows, parallax velocities are linearly proportional to both distance from the camera line-of-sight and local free-stream velocity.

Figure 9 shows the mean cross-stream velocity field for the mixed-boundary corner without applying any parallax correction. One can clearly see that the inner secondary

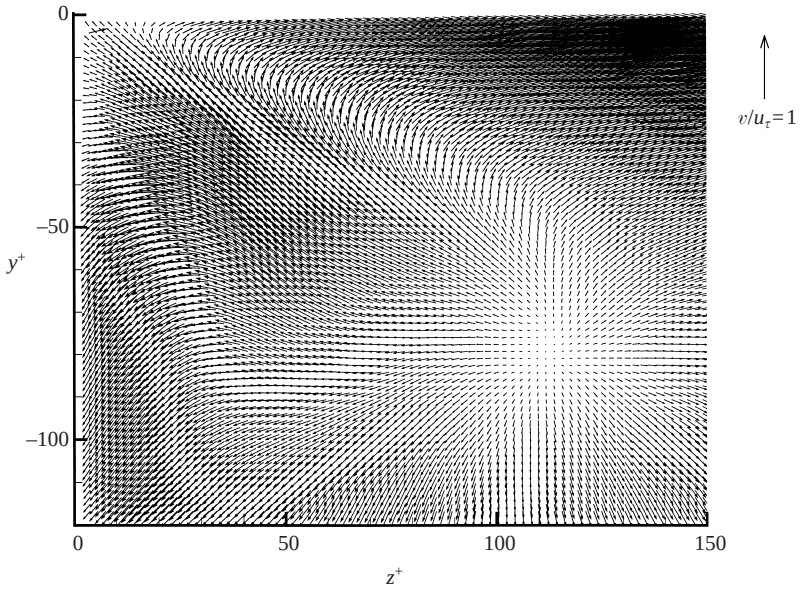

FIGURE 9. Uncorrected mean cross-stream velocity field.

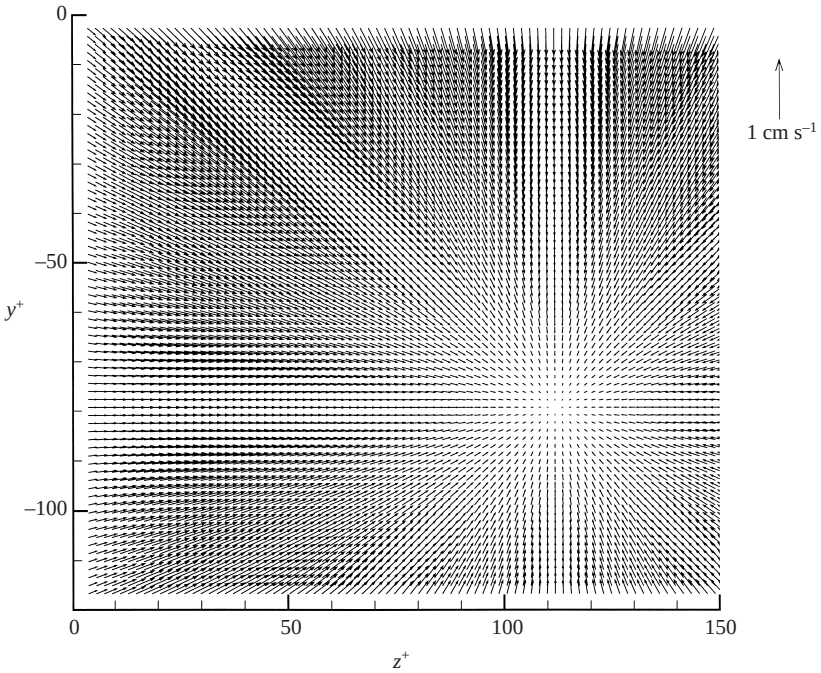

FIGURE 10. Parallax correction for the cross-stream mean velocity field including compensation for the mean streamwise boundary layer profile.

vortex is not visible and that there appears to be a non-physical source located at $y^+ \approx -80$ and $z^+ \approx 110$. Because the actual cross-stream velocities are on the same order as the parallax velocities, it can be assumed that the apparent source is actually the location of the line-of-sight of the camera.

A parallax velocity correction was developed using the location of the line-of-sight, identified in figure 9, and the mean turbulent boundary layer velocity profile presented in Hsu (1999) and Hsu *et al.* (2000). The resulting correction field is shown in figure 10. For simplicity, vertical variations in mean streamwise velocity were not included in the correction. One can see in the figure that the horizontal component of the parallax correction decreases on approaching the wall as a result of the no-slip boundary.

The final mean cross-stream velocity field, shown in figure 4, can be obtained by subtracting the parallax correction, figure 10, from the 'raw' mean cross-stream field, figure 9. In practice, the parallax correction was subtracted from each instantaneous velocity field. In this manner, the turbulence quantities shown in figures 5–8 also have the parallax effect removed.

Because the parallax correction was approximate, a 'dc' bias was introduced to the data. This is perhaps most evident in the cross-stream vectors closest to the free surface shown in figure 4. Note they all have a small downward component. Since the top row of vectors is not at the free surface, a small downward flow below the surface is indeed possible. In the inner secondary flow region, the magnitude of the downflow is $\sim 0.07\,\mathrm{cm\,s^{-1}}$. This is a reasonable estimate of the maximum parallax correction bias. Note that the bias will reduce to zero on approaching the camera line-of-sight. Though the bias is small, it does raise the issue of measurement uncertainties, particularly for the vorticity transport terms. This is addressed in the following Appendix.

Appendix B. DPIV measurement uncertainties

The principal goal in developing a DPIV processing program at Rutgers was to generate accurate, high-resolution vector fields for computing complex turbulence transport quantities. Unlike many commercial DPIV packages, accuracy was given paramount priority at potentially significant cost to computational speed. In this study, the robustness of the routine was severely tested by requiring accurate resolution of mean secondary motions, two orders of magnitude smaller than the free-stream speed. This Appendix addresses accuracy and uncertainty issues associated with the measurements reported in the main body of this paper.

Note at the outset that there are three classes of uncertainty in the measurements presented in this paper. The first is associated with convergence of stochastic processes (i.e. turbulent statistics) for finite sample sizes. The second uncertainty arises from the accuracy and resolution of the DPIV measurement technique. The third source of uncertainty is 'dc' bias resulting from the parallax correction algorithm outlined in Appendix A. This appendix is divided into four sub-sections. The first three address each of the specific classes of uncertainty just identified. The fourth provides uncertainties for all data shown in this paper with notes on how values were obtained.

B.1. *Incomplete convergence of turbulence statistics*

For the first class of uncertainties, ε, Lumley & Panofsky (1964) provide the following equation for determining the effect of finite sampling period for turbulence measurements:

$$\varepsilon = U_\infty \{2I(u'/U_{\mathrm{local}})^2/T\}^{1/2}. \tag{B 1}$$

Here I is the integral time scale of the flow, and T represents the total sampling time. In this case, the integral time scale can be estimated as δ/U_∞ where δ is the boundary

layer thickness. For this flow, the boundary layer thickness is approximately 5.7 cm for a free-stream velocity of 12 cm s^{-1}. In this case, then, the integral time scale is approximately 0.48 s. The sampling period is 2000 s, and u'/U_{local} is estimated to be 0.3. Substitution into (B 1) yields a value for ε of 0.078 cm s^{-1} or $\varepsilon^+ = 0.125$.

B.2. *DPIV particle displacement resolution experiment*

There is a range of uncertainty estimates in the literature for particle displacement resolution, e, ranging from $O(0.01)$ pixels at the low end, as proposed by Raffel, Willert & Kompenhans (1998), to the more commonly accepted $O(0.1)$ pixel uncertainty put forward by Keane & Adrian (1992, 1993). Their typical uncertainty was reported as ~ 0.05 pixels.

During its development, the current DPIV system was calibrated using a series of steps including translation and rotation of a pattern of dots as well as solid-body rotation of seeding particles in water. These tests are described in Hsu (1999). Further benchmarking of this capability for turbulent energy transport in the mixed boundary corner appears in Hsu *et al.* (2000). In that study, turbulent kinetic energy production, dissipation and diffusion profiles were obtained which matched DNS calculations. They proposed that the accuracy of the current DPIV system appears to be better than 0.02 pixels.

Ultimately, the validity (and believability) of the uncertainty analyses presented in Hsu (1999) and Hsu *et al.* (2000) depends heavily on assumptions made about the sub-pixel accuracy of the DPIV algorithm. To better assess the accuracy of the current DPIV system, therefore, an experiment involving direct measurements was conducted. The experiment entailed obtaining 1000 DPIV velocity vector fields at a fixed location in the laminar, potential-core region of the water-tunnel test section. Since the flow is not, in fact, perfectly laminar, variations in velocity measurements may arise from free-stream turbulence, DPIV uncertainty or mean spatial non-uniformity. To simplify the analysis (and to err on the conservative side), variations in this data set were attributed entirely to DPIV uncertainty.

B.2.1. *Mean particle displacement uncertainty*

With this simplifying assumption, measurement uncertainties were evaluated. First, the convergence of the mean was examined as a function of the number of vector fields in an ensemble. This is plotted in figure 11 for two different locations in the vector fields. One can see that the mean pixel displacement in the x-direction, Δx, appears to be well-converged with 1000 vector fields. A conservative estimate of the uncertainty in Δx is ± 0.002 pixels for an ensemble size, N, greater than 700. For the current field of view and time between images, this corresponds to 0.00115 cm s^{-1}. By comparison, the uncertainty due to lack of convergence of finite sample turbulence measurements was almost two orders of magnitude larger, $\varepsilon \approx 0.078$ cm s^{-1}.

B.2.2. *R.M.S. particle displacement uncertainty*

To estimate turbulence intensity uncertainties, the root-mean-square deviation in x-component particle-displacement measurements were computed using the potential-flow data set. This was done by computing the r.m.s. of Δx measurements taken from the same spatial location in each of the 1000 vector fields. Several different locations were used to ensure spatial uniformity. The r.m.s. particle-displacement uncertainty was found to be ~ 0.0165 pixels. It is worth noting that this matches the estimate presented in Hsu *et al.* (2000). In terms of the present experiment, this corresponds to 0.0095 cm s^{-1}.

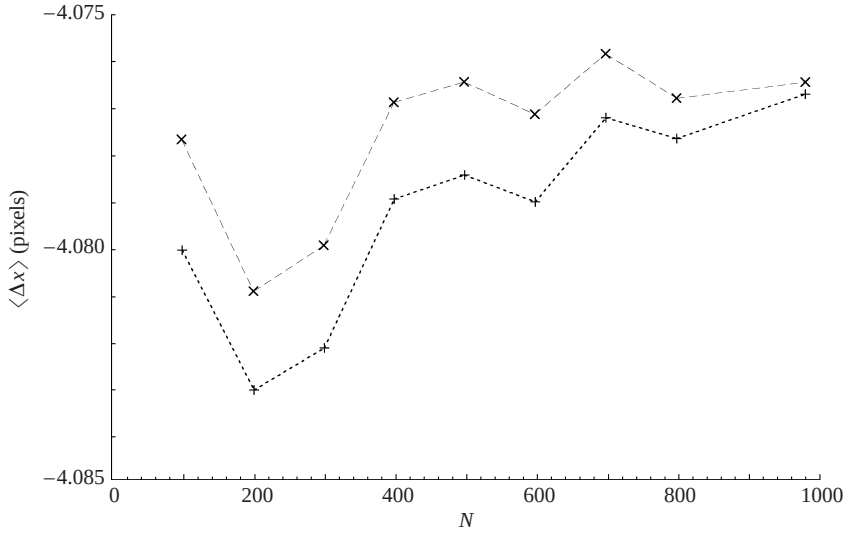

FIGURE 11. Convergence of mean particle displacement calculations for 1000 DPIV measurements made in the potential laminar core of the test section, for two different locations.

B.2.3. *Reynolds stress uncertainty*

It would seem reasonable to assume that uncertainties associated with orthogonal velocity components would be uncorrelated. That is, one would expect that the uncertainty in Reynolds stress measurements due to DPIV error should be small. This was in fact the case for the current system. The cross-correlation between horizontal and vertical particle displacement measurements, $\langle \Delta x \Delta y \rangle$ was computed for the 1000 potential-flow vector fields at fixed spatial locations. Like the r.m.s. measurements, Reynolds stress uncertainties were calculated at a number of spatial locations. $\langle \Delta x \Delta y \rangle$ was found to be $\sim 3.6 \times 10^{-5}$ pixels^2, corresponding to uncertainties in the measured Reynolds stress, $\langle uv \rangle$, of $\pm 1.2 \times 10^{-5}$ (cm s^{-1})^2.

B.2.4. *Uncertainty in spatial gradients*

Each term in the vorticity transport equations, (1) or (2), contains ensemble averages of spatial velocity derivatives. The usefulness of the transport terms shown in each plot comprising figure 8, therefore, is directly a function of the uncertainty of $\partial u_i/\partial x_j$ and $\partial^2 u_i/\partial x_j^2$. These uncertainties could also be computed from the potential laminar flow data set.

Using central differences, uncertainties in $\langle \partial u_i/\partial x \rangle_j$ and $\langle \partial^2 u_i/\partial x_j^2 \rangle$ were found to be 1.0×10^{-5} pixels/pixel and 1.5×10^{-7} pixels/pixel^2, respectively. In dimensional form, these uncertainties correspond to 9.4×10^{-5} s^{-1} and 2.3×10^{-5} cm^{-1} s^{-1}. Like the previous quantities, § B.2.2 and § B.2.4, uncertainties in spatial derivatives were computed using the same spatial location in each of the 1000 independent vector fields. Again, several locations were examined to ensure uniformity across the measurement field.

Clearly, uncertainties in spatial derivatives are quite small, which may be explained in terms of the four-times oversampling used by the particle displacement algorithm. Consider an arbitrary vector location. Vectors on either side of this location were computed using interrogation windows with 50% overlap. Any errors from the

correlation routine would tend to be biased in the same direction. Thus, uncertainties in local gradients are inherently small in DPIV.

B.3. *Parallax correction uncertainties*

Uncertainties associated with the parallax correction developed for this study were introduced in Appendix A. These arise principally because of the approximate boundary layer velocity profile used to account for non-uniform flow through the illuminating laser sheet. Ideally, instantaneous streamwise velocity data would be needed across the entire cross-stream field of view when each vector field was obtained.

The maximum magnitude of this bias was estimated to be $0.07\,\mathrm{cm\,s^{-1}}$ along the top row of vectors in figure 10. Such a correction would make the vertical velocity at the free surface in the inner secondary flow region zero. It was also noted that this bias uncertainty would decrease to zero at the camera's line-of-sight.

The impact of parallax correction bias on secondary vortex data presented in this paper lies primarily in mean velocities and mean velocity gradients. The maximum bias in mean spatial gradients is estimated to be $0.035\,\mathrm{s^{-1}}$ ($0.07\,\mathrm{cm\,s^{-1}}$ divided by $\sim 2\,\mathrm{cm}$ distance between the point of maximum bias to the camera line-of-sight). While turbulence fluctuation data, such as r.m.s. and Reynolds stresses, would also be affected (because the correct mean velocities could not be subtracted from the instantaneous measurements), this effect is arguably quite small because the maximum bias is small relative to the instantaneous cross-stream velocities.

B.4. *Uncertainties in the turbulence and vorticity transport data*

Having quantified the different classes of uncertainty in this experiment, it is now possible to calculate uncertainties in measured and derived quantities presented in the body of this paper. A summary of all uncertainties appears in table 1, including those outlined throughout this Appendix. Note that bias uncertainties due to the parallax correction are listed separately from random statistical uncertainties due to DPIV and incomplete convergence, etc. Two uncertainty values are provided. The first are actual estimates non-dimensionalized by kinematic viscosity and the nominal friction velocity, $0.63\,\mathrm{cm\,s^{-1}}$. The second uncertainty values, in parenthesis, are estimates of percent uncertainty relative to the maximum values for the flow. For example, the uncertainty for mean cross-stream velocities, $0.078\,\mathrm{cm\,s^{-1}}$, becomes 0.125 when non-dimensionalized by friction velocity. In turn, this is $\sim 10\%$ of the maximum value of W shown in figure 4. Maximum values for higher-order turbulence quantities, such as vorticity gradients, were estimated by examination of contour plots, such as figure 5.

Uncertainties associated with complex quantities, such as the vorticity transport equation, were computed using a few simple rules. First, products or quotients of quantities were assumed to have uncertainties equal to the sum of the component uncertainties. Second, based on the uncertainty analysis work of Kline & McClintock (1953), the total uncertainty in a multiple uncertainty measurement equals the square root of the sum of the individual uncertainties squared. Finally, uncertainties in mean gradients of fluctuating quantities, e.g. $\partial u_i^+/\partial x_j^+$ and $\partial \omega_x^+/\partial x_j^+$, were computed by multiplying the uncertainty of the dependent variable by $\sqrt{2}$ and dividing by four times the vector spacing. Although central differences are computed over twice the vector spacing, four vector spacings were used in the uncertainty calculation because of the four-times oversampling used in the DPIV algorithm. Every fourth vector is statistically independent.

For example, the uncertainty of mean spatial gradients of u_i^+, i.e. $\partial u_I^+/\partial x_j^+$, were estimated by multiplying the uncertainty in u_i^+ ($= 0.015$) by $\sqrt{2}$ and dividing by four

Turbulence quantity	Maximum bias uncertainty	Statistical uncertainty
Mean velocities U_i/u_τ	0.11 (9%)	0.125 (10%)
Mean velocity gradients $\partial U_i^+/\partial x_j^+$	0.0018 (16%)	2.4×10^{-6} ($\sim 0\%$)
Mean vorticity gradients $(\partial/\partial x_j^+)\{\partial U_i^+/\partial x_j^+ - \partial U_i^+/\partial x_j^+\}$	~ 0 ($\sim 0\%$)	9.2×10^{-9} ($\sim 0\%$)
Turbulence intensities u_i/u_τ	~ 0 ($\sim 0\%$)	0.015 (1.5%)
Fluctuating velocity gradients $\partial u_i^+/\partial x_j^+$	~ 0 ($\sim 0\%$)	0.0033 (11%)
Fluctuating vorticity gradients $(\partial/\partial x_j^+)\{\partial u_i^+/\partial x_j^+ - \partial u_i^+/\partial x_j^+\}$	~ 0 ($\sim 0\%$)	0.00072 (24%)
Reynolds stresses $-\langle u_i u_j\rangle/u_\tau^2$	~ 0 ($\sim 0\%$)	3.0×10^{-5} ($\sim 0\%$)
Mean vorticity advection $U_j^+ \partial \Omega_i^+/\partial x_j^+$	2.7×10^{-4} (9%)	3.0×10^{-4} (10%)
Mean reorientation/stretching $\Omega_j^+ \partial U_i^+/\partial x_j^+$	0.0012 (39%)	~ 0 ($\sim 0\%$)
Vorticity diffusion $\nu \partial^2 \Omega_i^+/\partial x_j^{+2}$	~ 0 ($\sim 0\%$)	~ 0 ($\sim 0\%$)
Mean vorticity advection $u_j^+ \partial \omega_i^+/\partial x_j^+$	~ 0 ($\sim 0\%$)	7.5×10^{-4} (25%)
Mean reorientation/stretching $\omega_j^+ \partial u_j^+/\partial x_j^+$	~ 0 ($\sim 0\%$)	8.1×10^{-4} (27%)

TABLE 1. Summary of bias and statistical uncertainties for turbulence and vorticity transport data presented in this paper.

times the non-dimensional vector spacing. (The $\sqrt{2}$ reflects that the differential ∂u_I is the difference of two velocity values, each with identical uncertainty. From Kline & McClintock (1953), then, the uncertainty in ∂u_I is the square root of the sum of the squares of the individual uncertainties, or $\sqrt{2}$ times the uncertainty in u_I^+.) In turn, the uncertainty in the ensemble-averaged fluctuating vorticity is $\sqrt{2}$ times the uncertainty in $\partial u_I^+/\partial x_j^+$. And finally, the uncertainty in reorientation/stretching term due to fluctuating quantities is the sum of the uncertainties of ω_j^+ and $\partial u_I^+/\partial x_j^+$. Note that uncertainties for terms in the turbulent vorticity transport equation are given only in terms of percentages. These were calculated using the percentage uncertainties of the component quantities.

As a test of the uncertainty calculations, comparisons between present measurements and data from Hsu *et al.* (2000) are shown in figures 12 and 13. Figure 12 shows profiles of mean wall-normal velocity, W^+, as a function of distance from the wall, z^+, for different distances below the free surface. Figure 12(b) contains profiles extracted from the present data shown in figure 4, while figure 12(a) contains similar data presented in Hsu *et al.* (2000). The latter data were obtained using DPIV in measurement planes parallel to the free surface.

The similarities between data sets are immediately obvious. There is agreement in both the absolute numerical values as well as trends. There are, of course, differences; the maximum values of W^+ are larger for the present measurements, for example. The bias introduced by the parallax correction as well as incomplete convergence

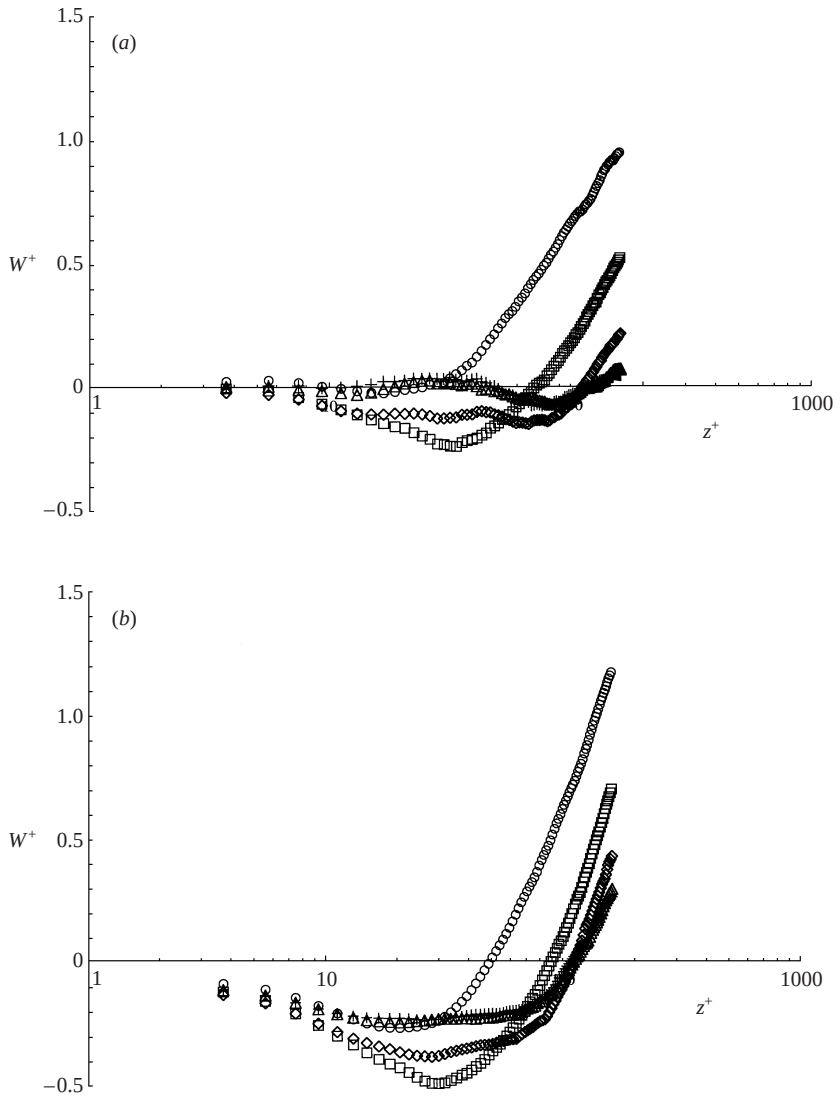

FIGURE 12. Comparison of mean wall-normal velocity profiles, W^+ vs. z^+ from (a) Hsu *et al.* (2000) and (b) present measurements. ○, $y^+ = -19$; □, $y^+ = -38.5$; ◇, $y^+ = -56.4$; △, $y^+ = -76.0$; +, $y^+ = -95.6$.

of the statistics account for most of these differences. However, one should also recognize that there are uncertainties in assigning the free-surface location, and there were probably differences in tunnel speed, water temperature, and other controlling parameters between the two data sets. The time between acquisition of the two sets was over a year.

Agreement between profiles of w'/u_τ is also quite strong. These are shown in figure 13. Again, data from the present study and from Hsu *et al.* (2000) are shown in figures 13(a) and 13(b), respectively. Like the mean velocity counterparts, there is excellent agreement between the two data sets. While the trends for different distances below the free surface are also consistent between data sets, there is some difference in magnitudes of w'/u_τ particularly for the profiles farthest from the free

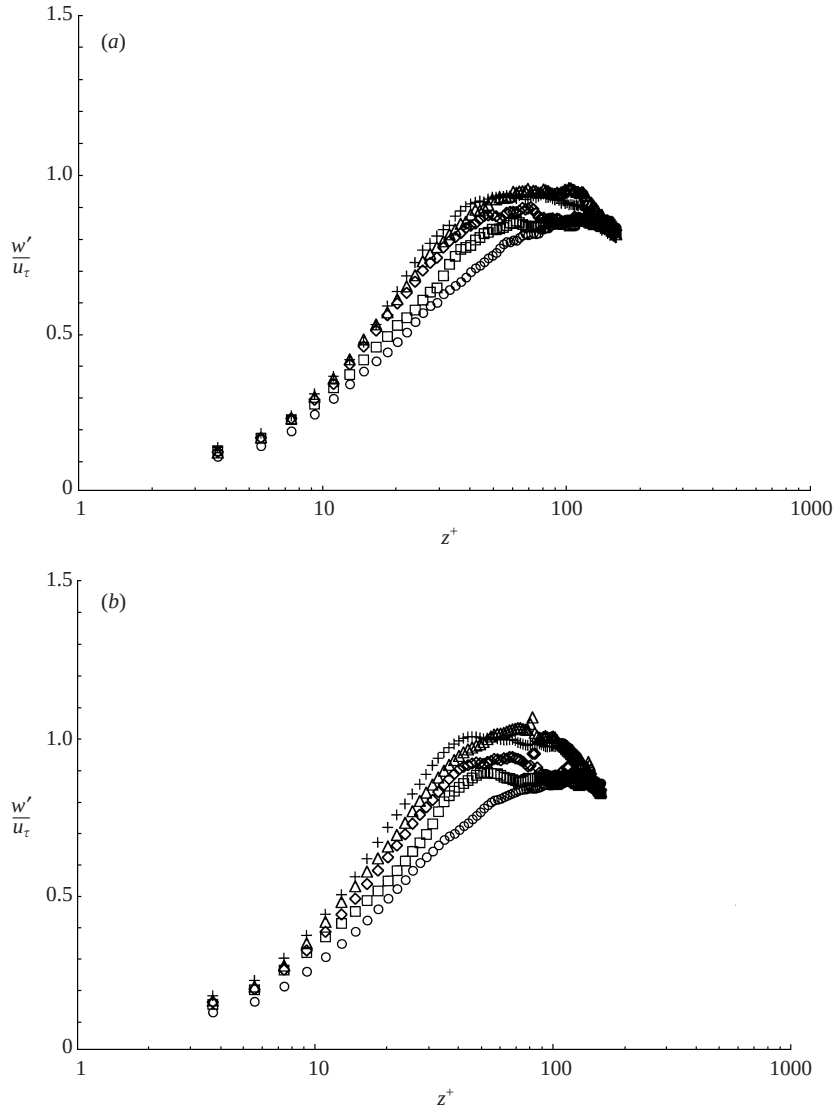

FIGURE 13. Comparison of fluctuating wall-normal velocity profiles, w'/u_τ vs. z^+ from (*a*) Hsu *et al.* (2000) and (*b*) present measurements. See caption figure 12 for symbols.

surface. This may be a manifestation of differences in determining the wall and free-surface locations, in the mean values propagating into the r.m.s. calculation, or simply differences in flow conditions between the two experiments.

Ultimately, the smoothness of the data and the ability to discern clear trends between different spatial positions confirms the uncertainty limits presented in this Appendix. The same techniques were used in Hsu *et al.* (2000) to compute terms in the turbulent kinetic energy transport equation with similar success. There is certainly sufficient accuracy in the present data to resolve the inner and outer secondary flows hypothesized in earlier works, and to shed light on the origins of these flows.

REFERENCES

Anthony, D. G. & Willmarth, W. W. 1992 Turbulence measurements in a round jet beneath a free surface. *J. Fluid Mech.* **243**, 699.

Gessner, F. B. & Jones, J. B. 1961 A preliminary study of turbulence characteristics of flow along a corner. *Trans. ASME* D: *J. Basic Engng* **83**, 657.

Gessner, F. B. & Jones, J. B. 1965 On some aspects of fully-developed turbulent flow in rectangular channels. *J. Fluid Mech.* **23**, 689.

Grega, L. M. 1995 Generation of secondary flows in turbulent flow along a solid wall-free surface corner. PhD Dissertation, Rutgers University.

Grega, L. M., Wei, T., Leighton, R. I. & Neves, J. C. 1995 Turbulent mixed-boundary flow in a corner formed by a solid wall and a free surface. *J. Fluid Mech.* **294**, 17.

Hsu, T. Y. 1999 Turbulent transport in the mixed-boundary corner formed by flow along a solid wall close to a free surface. MS Thesis, Rutgers University.

Hsu, T. Y., Grega, L. M., Leighton, R. I. & Wei, T. 2000 Turbulent kinetic energy transport in a corner formed by a solid wall and a free surface. *J. Fluid Mech.* **410**, 343.

Keane, R. D. & Adrian, R. J. 1992 Theory of cross-correlation analysis of PTV images. *Appl. Sci. Res.* **49**, 191.

Keane, R. D. & Adrian, R. J. 1993 Prospects for super-resolution with particle image velocimetry. *Proc. SPIE; Opt. Diag. Fluid Therm. Flow* **2005**, 283.

Kline, S. J. & McClintock, F. A. 1953 Describing uncertainties in single-sample measurements. *Mech. Engng* **75**, 3.

Logory, L. M., Hirsa, A. & Anthony, D. G. 1996 Interaction of wake turbulence with a free surface. *Phys. Fluids* **8**, 805.

Longo, J., Huang, H. P. & Stern, F. 1998 Solid/free surface juncture boundary layer and wake. *Exps. Fluids* **25**, 283.

Lumley, J. L. & Panofsky, H. A. 1964 *The Structure of Atmospheric Turbulence*. Interscience.

Raffel, M., Willert, C. E. & Kompenhans, J. 1998 *Particle Image Velocimetry*. Springer.

Sarpkaya, T. 1996 Vorticity, free surface, and surfactants. *Annu. Rev. Fluid Mech.* **28**, 83.

Smith, G. B. 1992 Turbulent cascade in colliding off-axis vortex rings. MS Thesis, Rutgers University.

Sreedhar, M. & Stern, F. 1998 Large eddy simulation of temporally developing juncture flows. *Intl J. Numer. Meth. Fluids* **28**, 47.

Tennekes, H. & Lumley, J. L. 1972 *A First Course in Turbulence*. MIT Press.

Thomas, T. G. & Williams, J. J. R. 1995 Large eddy simulation of turbulent flow in an asymmetric compound open channel. *J. Hydraul. Res.* **33**, 27.

Walker, D. T., Leighton, R. I. & Garza-Rios, L. O. 1996 Shear-free turbulence near a flat free surface. *J. Fluid Mech.* **320**, 19.